JPhys Materials

PAPER • OPEN ACCESS

Manganese and cobalt substituted ferrite nanoparticles synthesized via a seed-mediated drip method

View the article online for updates and enhancements.

Journal of Physics: Materials

PAPER

Manganese and cobalt substituted ferrite nanoparticles synthesized via a seed-mediated drip method

Zichun Yan[1] , Sara FitzGerald[2] , Thomas M Crawford[2] and O Thompson Mefford[1,*]

1 Department of Materials Science and Engineering, Clemson University, Clemson, SC 29634, United States of America
2 Department of Physics and Astronomy, SmartState Center for Experimental Nanoscale Physics, University of South Carolina, Columbia, SC 29208, United States of America
* Author to whom any correspondence should be addressed.

E-mail: mefford@clemson.edu

Abstract

To produce multi-dopant ferrite nanoparticles, the 'Extended LaMer' and seed-mediated growth techniques were combined by first utilizing traditional thermal decomposition of metal acetylacetonates to produce seed particles, followed by a continuous injection of metal oleate precursors to increase the volume of the seed particles. With the choice of precursors for the seeding and dripping stage, we successfully synthesized particles with manganese precursor for seeding and cobalt precursor for dripping ($Mn_{0.18}Co_{1.04}Fe_{1.78}O_4$, 17.6 ± 3.3 nm), and particles with cobalt precursors for seeding and manganese precursors for dripping ($Mn_{0.31}Co_{0.74}Fe_{1.95}O_4$, 19.0 ± 1.9 nm). Combining transmission electron microscopy, energy-dispersive x-ray spectroscopy, x-ray diffraction, and vibrating sample magnetometry, we conclude that the seed-mediated drip method is a viable method to produce multi-dopant ferrite nanoparticles, and the size of the particles was mostly determined by the seeding stage, while the magnetic properties were more affected by the dripping stage.

1. Introduction

Over the past few decades, magnetic nanoparticles have been extensively developed as potential devices for medical applications, such as magnetic hyperthermia, MRI, magnetic particle imaging, and drug delivery, etc [1–5]. Iron oxide-based nanoparticles have drawn tremendous attention because of the ease of synthesis, moderate biocompatibility, and good tunability of the properties [6, 7]. Thermal decomposition is one of the most commonly used synthetic approaches for making iron oxide-based nanoparticles [8]. It generally offers good control of the size and composition of the particles, thus it also provides precise control of the magnetic properties of the nanoparticles [9–11]. To synthesize iron oxide-based nanoparticles with various sizes and compositions, methods with metal fatty acid salts or metal acetylacetonate salts as precursors have been developed [12, 13]. The appeal of these synthetic routes is that to control the size and composition of the final product, only concentration or relative ratios of precursors, solvents, and surfactants need to be changed while not requiring the alteration of the reaction temperature. Apart from a one-pot reaction, reactions with continuous addition of precursors were also developed to enhance the size control of the nanoparticles [14–16]. This method extended LaMer's mechanism and achieved continuous growth of the particles by feeding precursors throughout the reaction without changing the starting stage of the reactions.

Beyond controlling the size of the particles, some researchers have developed methods to control the magnetic properties of the nanoparticles by changing the composition of particles. As thoroughly explained by López-Ortega *et al* [17] and Liu *et al* [18], nanoparticles containing both soft and hard magnetic phases potentially expand the selection pool of iron oxide-based nanomaterials significantly by broadening the range of magnetic properties of the ferrites through exchange coupling. Previous studies have shown great promise in using a core/shell exchange-coupled structure design to improve the magnetic properties of the

nanoparticles and thus their performance for specific applications [19–23]. It is worth noting that all these core/shell particles were synthesized via a seed-mediated growth method similar to the method which Shouheng Sun *et al* used for controlling the size of the particles [12]. The mechanism was to separate the nucleation stage from the growth stage of the particles to achieve a narrow size distribution; therefore, a typical seed-mediated particle synthesis requires multiple steps of reaction and purification.

Our research group previously has reported using an 'extended LaMer' method (also described as the drip synthesis) to successfully produce cobalt ferrite nanoparticles with narrow size distribution [24]. Herein, we describe the combination of the conventional seed-mediated synthesis with the drip synthesis (seed-mediated drip synthesis) to make manganese and cobalt substituted ferrite particles. This method significantly decreased the complexity of the whole synthesis process without having to stop at the first stage of seed particle synthesis. The growth of the particles and the incorporation of each metal element were monitored, and the final products were characterized afterward.

2. Experimental methods

2.1. Metal oleate precursor synthesis
The metal oleate precursors were synthesized by a reflux reaction. Forty millimoles cobalt (II) chloride (97% anhydrous, Acro Organics) or manganese (II) chloride (97% anhydrous, Acro Organics), 80 mmol sodium oleate (97%, TCI America), 80 ml ethanol (denatured ACS, VWR Chemicals BDH), 60 ml deionized water (DI water) and 140 ml hexane (mixture of isomers, 98.5% ACS, VWR Chemicals BDH), were mixed and heated to reflux. Once the temperature stopped rising, the reflux was kept at that temperature for 4 h. The upper organic layer (hexanes) was collected separating from the lower aqueous layer using a separatory funnel and washed with DI water three times after the reaction was completed. The hexane was then evaporated off using rotovap and the resulting viscous liquid product was then washed with acetone and precipitated by centrifugation (10 000 rpm, 10 min) several times until a clear supernatant was obtained. The final precipitation was dried in a vacuum oven at room temperature for 24 h yielding a waxy solid with a purple (cobalt oleate) and a brown (manganese oleate) color. The solid oleate precursors were then dissolved in 1-octadecene (tech 90%, Acro Organics) to make 0.1 mmol ml^{-1} solutions for injection.

2.2. Thermal gravimetric analysis (TGA) of precursors and pre-synthesis experiments
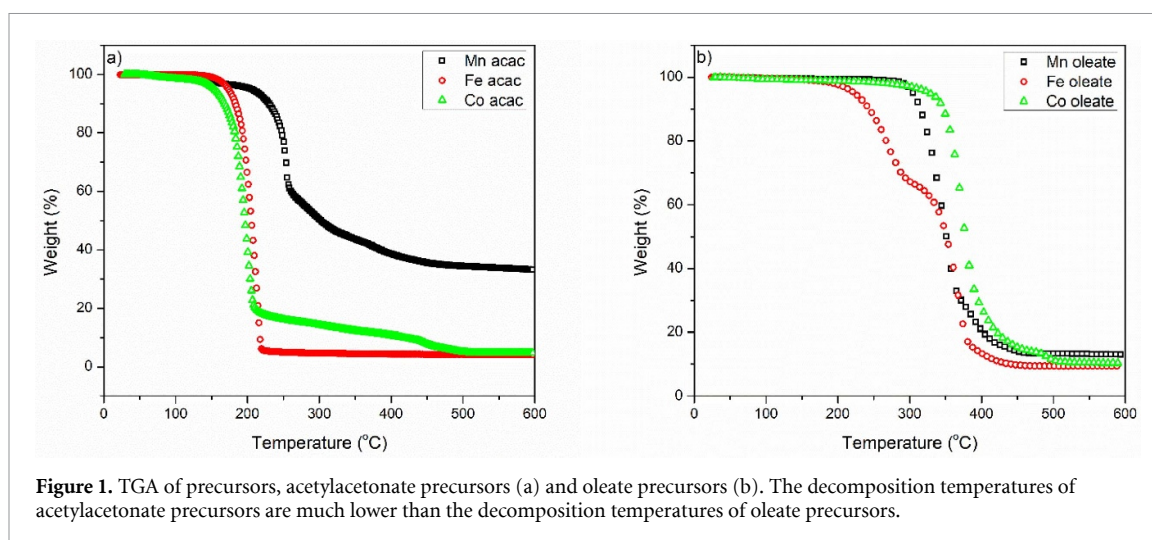Before synthesizing the nanoparticles, TGA of precursors was done to obtain the decomposition temperature of each precursor. Then, a set of control experiments to synthesize particles with a composition of $Mn_{0.5}Co_{0.5}Fe_2O_4$ was done to choose a good combination of precursors and conditions for monodisperse particles. Five batches of reactions were done with 2 mmol of iron precursor, 0.5 mmol of manganese precursors, and 0.5 mmol of cobalt precursors. The acetylacetonate (acac) and oleate precursors were added to the reaction flask before reaction (one-pot) or via injection while heating (drip) and the reactions were kept at 360 °C for 100 min. TGA of the precursors was done under nitrogen from room temperature to 600 °C with a ramping rate of 20 °C min^{-1}. The data was analyzed using the TA Universal Analysis software.

2.3. Seed and drip synthesis of core/shell particles
A manganese ferrite/cobalt ferrite core/shell structure was targeted for particle synthesis. The reaction consists of two stages, the first stage of the seeding reaction process was first done followed by the second stage of the injection of oleate precursors. To make particles with manganese-rich core and cobalt-rich shell (MnFe + Co), 2 mmol iron (III) acetylacetonate (99+%, Acro Organics), 0.5 mmol manganese (II) acetylacetonate (Sigma-Aldrich) were mixed with 0.3 g 1,2-hexadecanediol (tech. 90%, Sigma-Aldrich), 3 ml oleic acid (tech. 90%, Alfa Aesar) in a 100 ml flask and heated at 360 °C for 40 min. Then, the second precursor solution of cobalt oleate was injected into the reaction at 10 ml h^{-1} for 1 h. Aliquots were taken every 20 min to monitor the growth of the particles. In the same way, particles with cobalt-rich core and manganese-rich shell particles (CoFe + Mn) were also made by starting with cobalt (II) acetylacetonate (99%, Acro Organics) followed by the injection of manganese oleate. The reactions were done under a continuous flow (0.3 l min^{-1}) of nitrogen gas. After the reaction, the particles were washed with ethanol and precipitated by centrifugation (10 000 rpm, 5 min). The precipitation was then dissolved in hexane or dried under vacuum for later sample preparation for characterization.

2.4. Characterization methods
Transmission electron microscopy (TEM) images were acquired mainly using a Hitachi HT7830 at 120 kV. The images were analyzed for particle size distribution by Image J (NIH, open-source) with a minimum of 300 particles. Energy-dispersive x-ray spectroscopy (EDX) mapping was done using a Hitachi SU9000EA at 30 kV. The grids were pre-incubated in a vacuum oven at 80 °C overnight and treated with a UV cleaner to

Figure 1. TGA of precursors, acetylacetonate precursors (a) and oleate precursors (b). The decomposition temperatures of acetylacetonate precursors are much lower than the decomposition temperatures of oleate precursors.

Table 1. Decomposition temperature of precursors acquired from TGA.

Precursor	Decomposition temperature (°C)	Precursor	Decomposition temperature (°C)
Mn acac	242	Mn oleate	319
Fe acac	192	Fe oleate	348
Co acac	180	Co oleate	353

remove excess organic layers before the measurement. The measured area was selected and monitored in a high-angle annular dark-field scanning TEM mode.

Powder x-ray diffraction (XRD) was performed with a Rigaku Ultima IV diffractometer. The particles were well dispersed in hexane (approximately 50 mg ml^{-1}) and then dropped on the glass substrate and the particles deposited on it after the evaporation of the solvent. All samples were scanned with 0.5° min^{-1} from 15° to 80° with a copper Kα x-ray ($\lambda = 1.54$ Å). The XRD results were analyzed using Profex [25, 26].
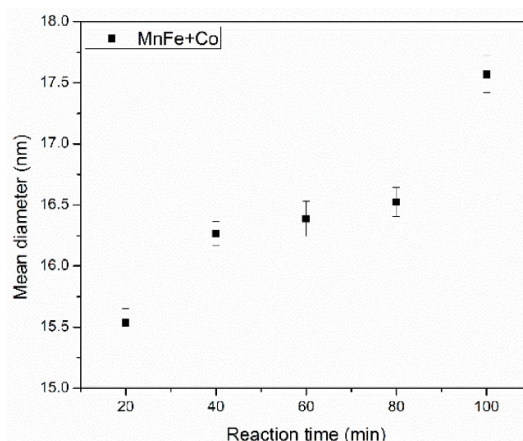
The magnetometry was done using the vibrating sample magnetometry (VSM) option of a physical property measurement system (Quantum Design). Magnetization-field (M–H) curves were measured at 300 K; zero-field cooling/field cooling (ZFC/FC) measurement was done with a 100 Oe (7980 A m^{-1}) magnetic field. The samples were made by curing the particle samples into a polymer matrix. Briefly, a stock solution of a mixture of monomers and initiator was made by mixing 3 ml of styrene (⩾99%, Sigma-Aldrich), 450 μl of divinylbenzene (tech. 80%, Sigma-Aldrich), and 10 mg of azobisisobutyronitrile (98%, Sigma-Aldrich). Then the dried particles were dissolved into this stock solution with a concentration of 6 mg ml^{-1}. Then the particle solution was cured inside a glass tube with an inner diameter of 1.5 mm and length of 3 cm at 90 °C for 1 h. The glass sheath was cracked, and the plastic/particle sample was cut into a 4 mm long pellet that was then mounted to the VSM sample holder.

The samples in polymer matrix after VSM measurement were decomposed at 500 °C and dissolved with 20 ml 2% nitric acid. The quantity of each element in the samples was determined through calibration curves constructed with corresponding standards with inductively coupled plasma (ICP) optical emission spectroscopy (OES). The results were then compared with the elemental analysis from EDX results and used for normalizing the data of VSM.

3. Results and discussion

3.1. Determination of synthetic approach
The TGA results are shown in figure 1 and table 1. The manganese precursors have the highest decomposition temperature among the acetylacetonate precursors and the lowest decomposition temperature among the oleates precursors, while the cobalt precursors have the lowest decomposition temperature among the acetylacetonate precursors and the highest decomposition temperature among the oleate precursors. This trend may be due to the electron affinity difference among the three metal cations. The reaction temperature of the synthesis was chosen at 360 °C, mainly because the decomposition of cobalt oleate happens at around 353 °C. A reaction temperature higher than the decomposition temperature of the precursor is necessary to assure a rapid decomposition of the precursors and successful incorporation of the metals.

Figure 2. Particle growth analysis of MnFe + Co sample from TEM. The mean diameter at the end of seeding stage (40 min) was 16.3 ± 3.4 nm, and the mean diameter at the end of dripping stage (100 min) was 17.6 ± 3.3 nm.

To make $Mn_{0.5}Co_{0.5}Fe_2O_4$ particles, five candidate approaches were tested. Different types of precursors or precursor solutions were added successively or at once (detailed procedures and TEM images can be found in the SI (available online at stacks.iop.org/JPMATER/4/034013/mmedia)). The approach with a one-pot seeding reaction with acetylacetonate precursors followed by the injection of oleate precursor was found to give the best monodispersity. The precursors of different metal species decompose at different temperatures; thus, the decomposition rates differ at a certain reaction temperature. The TGA results indicated acetylacetonate precursors have generally lower decomposition temperatures than the oleates; therefore, acetylacetonates were selected as the starting precursors for the seeding stage and oleates for the dripping stage, which can benefit the separation of nucleation and growth.
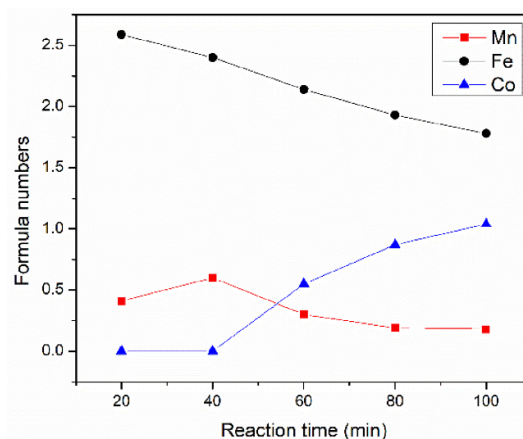
3.2. Seed-mediated drip synthesis of core/shell particles
To target the synthesis of core/shell nanoparticles, we chose manganese and cobalt as substituting metals, as these core/shell and soft/hard composite ferrite nanoparticles have been successfully made via conventional seed-mediated growth methods and have shown great potential for the application of magnetically modulated energy delivery [20, 27, 28]. Iron acetylacetonate and iron oleate are the two commonly used precursors [11]. We used the new seed-mediated drip synthesis method to produce two types of particles that may have core/shell structures by starting the seed reaction via decomposition of iron acetylacetonate along with manganese or cobalt acetylacetonate respectively, followed by the injection of oleate precursors of the other metal (acetylacetonates + oleate). The first stage of the 40 min seed reaction of metal acetylacetonates made monodisperse nanoparticles as seeds for the second stage of particle growth. When the second stage of precursor injection started at 40 min, the species of the reagents and their concentration changed and as a result, the growth of the particles was changed accordingly. Figure 2 illustrates the particle growth throughout the reaction for sample MnFe + Co. Nucleation was observed to start relatively fast, wherein the first 20 min of reaction had already provided particles of around 15.5 nm in diameter. The growth rate slowed down after 40 min. After a 60 min injection of the cobalt oleate precursor, the mean diameter of the particles grew from 16.3 ± 3.4 nm to 17.6 ± 3.3 nm. The TEM images and corresponding histograms of MnFe + Co samples are shown in the supporting information. The particles after 40 min, compared to 20 min, have a bimodal distribution which indicates an ongoing nucleation event. With the addition of a second precursor of cobalt oleate, both the small and large seeds started to grow larger after 40 min. This may be due to the decomposition temperature of Mn acac is about 50 °C higher than Fe acac. According to the size analysis we discussed above, assuming a core/shell structure, the mean shell thickness of the particles was about 0.65 nm (shell thickness $= \frac{\text{Final diameter} - \text{core diameter}}{2} = \frac{\text{diameter at 100 min} - \text{diameter at 40 min}}{2}$). Nonetheless, the same seed-mediated drip method was also used for making cobalt-rich core manganese-rich shell particles (CoFe + Mn), Co acac and Fe acac have very close decomposition temperatures, which led to more uniform nucleation and thus, more monodispersed particles (19.0 ± 1.9 nm) at the final stage (100 min). The size of the particles was mostly determined by the seeding stage of the synthesis and the species of the precursor of choice played a critical role in controlling the size distribution of the final product.
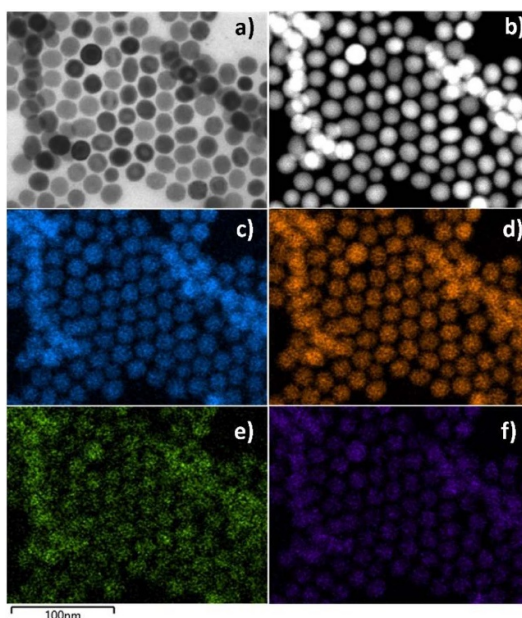
3.3. Structure analysis of the synthesized particles
The contents of each element in the MnFe + Co particles were analyzed by measuring aliquots via EDX. The compositional progression is shown in figure 3. The Mn/Fe ratio of the particle sample matches with the
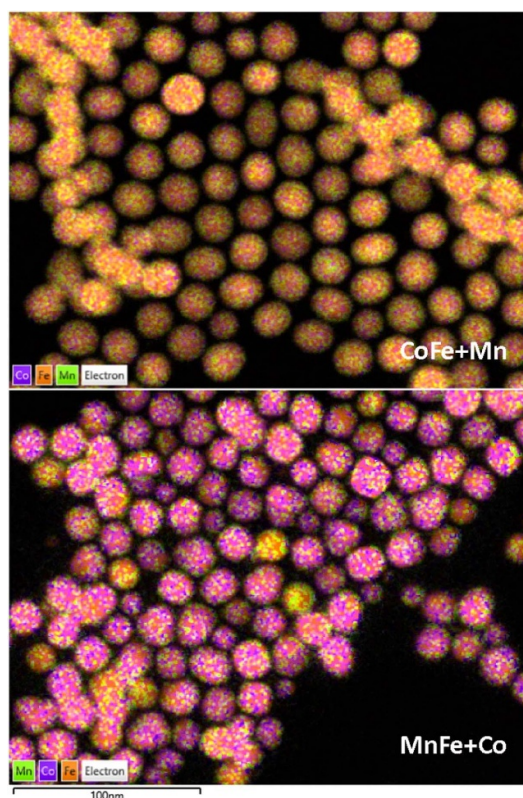
Figure 3. Composition evolution of MnFe + Co sample assuming a $Mn_xCo_yFe_{(3-x-y)}O_4$ formula. The composition at 40 min stayed the same as the feeding composition of acetylacetonate precursors. After 40 min, cobalt content increased while manganese content decreased, and reached a final composition of $Mn_{0.18}Co_{1.04}Fe_{1.78}O_4$ at 100 min.

Figure 4. EDX mapping of different elements of CoFe + Mn sample (a) BF image, (b) DF image, (c) oxygen, (d) iron, (e) manganese, (f) cobalt. All particles have the three metal elements, and the metal elements are uniformly distributed without showing a distinguishing core/shell structure.

starting precursor ratio at the end of the seeding stage within 40 min, however, after 40 min, the Co content started appearing in the particles and kept increasing through the rest of the reaction because of the injection of the cobalt oleate precursor. The Mn content kept decreasing with the injection of cobalt oleate after 40 min which was probably caused by the substitution of the Mn^{2+} ions by the Co^{2+}. Assuming the particles have a typical spinel ferrite $Mn_xCo_yFe_{(3-x-y)}O_4$ formula, the composition of the MnFe + Co particles grew from $Mn_{0.41}Co_0Fe_{2.59}O_4$ (20 min) to $Mn_{0.18}Co_{1.04}Fe_{1.78}O_4$ (100 min). Figure 4 shows the images gained from an elemental analysis via EDX mapping of sample CoFe + Mn after 100 min. The individual particles were seen, and all the metal elements were distributed through the particles. Figure 5 was generated by overlaying the mapping images of Mn, Fe, and Co, which shows the spatial distribution of the elements in the individual particles. For CoFe + Mn, and all three metals are distributed in all the particles, however, some of the MnFe + Co particles only have manganese and iron in them meaning that the second metal, cobalt, did not grow into/onto some of the seed particles. Interestingly, these manganese ferrite particles were not the smallest. Some particles contain cobalt seen smaller than those containing only manganese and iron. This means when the second stage of cobalt injection started at 40 min, the first stage of seed growth had not stopped, leading to a wider size distribution as the growth rate of the first stage is different from the second
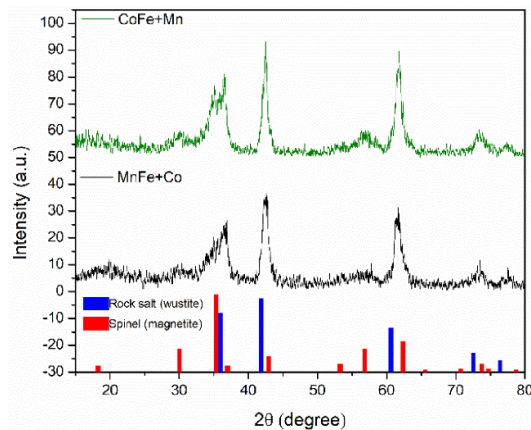
Figure 5. EDX mapping of metal elements of CoFe + Mn and MnFe + Co. CoFe + Mn particles are more monodispersed than MnFe + Co particles. Some of the particles in MnFe + Co samples have very low cobalt content indicating a nucleation process during the dripping stage.
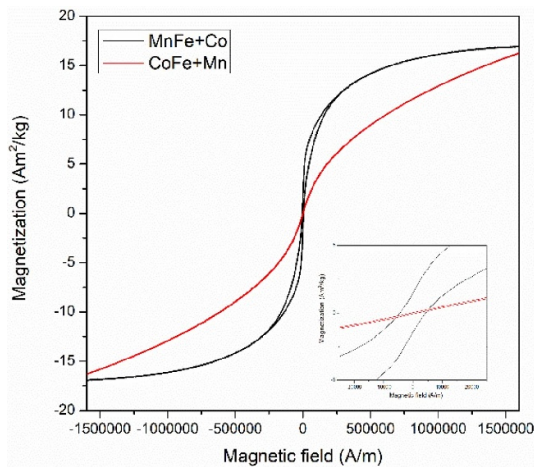
stage. Although the anticipated edge between the core and the shell was not seen in the EDX mapping images (figures 4, 5, and S1), the double-layer structure may still exist. For one thing, the thickness was too low to show a sharp interface; for another, the spherical shape of the particles made it harder to locate the interface between the core and the shell. The particle line scan image shows a clear shell with a thickness around 2.5 nm, but it was not seen in an EDX mapping image which suggests that this core/shell phase difference was not caused by the composition difference but by the difference in the oxidation states of the metal and the crystalline phases. A similar phenomenon was seen in the previous studies [15, 29–31]. The XRD analysis coincided with the EDX mapping and confirmed this hypothesis as shown in figure 6. The two samples both showed a ferrimagnetic spinel phase (magnetite PDF: 019-0629) as well as an antiferromagnetic rock salt (wüstite PDF: 00-006-0615) phase given the fact the final products did not undergo any post-reaction oxidation treatment. Further analysis of the XRD results (supporting information) showed that both samples have a significant fraction of the antiferromagnetic phase (37.1 wt% for MnFe + Co and 31.2 wt% for CoFe + Mn). Similar structures were also seen in other doped iron oxide nanoparticles synthesized with the thermal decomposition method [32–34]. The insufficient oxidation of the core is responsible for the rock salt phase and the shell of the particles was more oxidized resulting in a spinel structure shown in the XRD result. The existence of surface spin canting and the antiphase boundary is responsible for the reduction of magnetization which is prevalently seen for nanoparticles synthesized by thermal decomposition according to a previous study [35, 36].

3.4. Magnetic characterizations

The magnetization curve was measured at 300 K over the range of $\pm 1.6 \times 10^6$ A m^{-1} and plotted in figure 7. The magnetization values were normalized by the total mass of metals in the sample measured by ICP-OES. Although having close mean sizes (CoFe + Mn, 19.0 $\pm$ 1.86 nm; MnFe + Co, 17.6 $\pm$ 3.28 nm), the two samples behaved quite differently since the two samples have presumably different structures. The saturation magnetization and coercivity of sample MnFe + Co are both larger than CoFe + Mn which indicates the shell of the particles played a more important role in the magnetic properties. The MnFe + Co has a bias of -100 A m^{-1} and a coercivity of 4380 A m^{-1}, while CoFe + Mn has a bias of 400 and a coercivity of 1060 A m^{-1}. The existence of coercivity and bias at 300 K probably resulted from a weak exchange coupling between the rock salt core and the spinel shell [27, 37, 38]. The ZFC/FC measurement was done with a
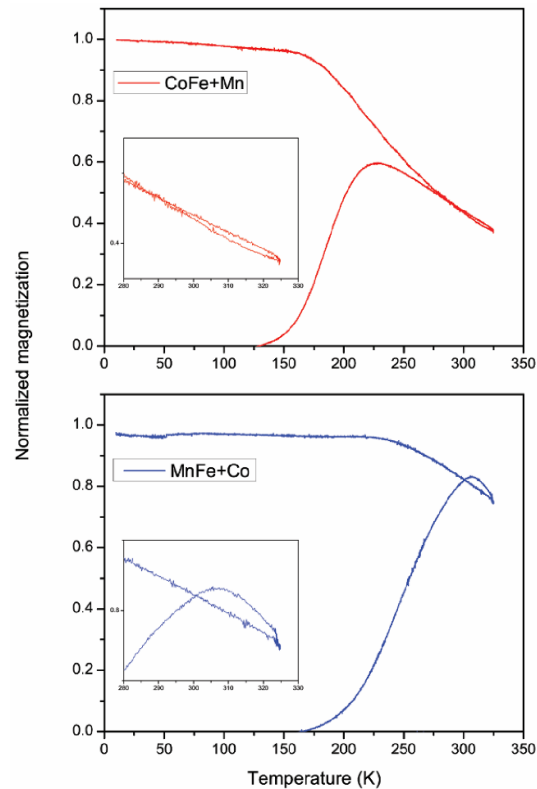
Figure 6. XRD diffractograms of CoFe + Mn and MnFe + Co samples. Both samples consist of ferrimagnetic spinel phase and antiferromagnetic rock salt phase.

Figure 7. Magnetization vs magnetic field (M–H) curve from VSM measurements. The magnetization values are much smaller than that of the bulk material because a large fraction of the nanoparticles does not contribute to the magnetic properties.

100 Oe (7980 A m^{-1}) magnetic field. The blocking temperature of each sample was estimated by taking the inflection point of the ZFC magnetization curves versus temperature. Historically, the blocking temperature has been taken as the peak of the ZFC curve. However, it has been shown that the mode blocking temperature is to the left of the peak and is more accurately determined by taking the inflection point of the ZFC curve. This is the temperature at which the greatest number of nanoparticle moments become unblocked or 'flip' to align with the applied field simultaneously, resulting in a rapid increase in the magnetic response of the sample according to Bruvera *et al* [39], and Livesey *et al* [40]. The results indicated the blocking temperature of the samples are 184 ± 7 K (CoFe + Mn) and 251 ± 13 K (MnFe + Co) respectively (detailed depiction refers to supporting information). The blocking temperatures of $CoFe_2O_4$ and $MnFe_2O_4$ particles of similar sizes are around 320 K and 170 K, respectively [41, 42]. These values match well with the previously reported blocking temperatures of manganese–cobalt substituted ferrite particles [27, 28]. Interestingly, we found that the ZFC curves (figure 8) for both samples have higher magnetization values than the FC curves above 300 K and this behavior of MnFe + Co was more prominent than that of CoFe + Mn. Such a behavior usually indicates the magnetostriction of the ferrite material, i.e. the change of dimension or movement of domain walls during magnetization [43, 44]. Such magnetostriction property is commonly seen in cobalt ferrite as it is used in magnetostrictive sensors or actuators [45]. The magnetic measurements showed that the magnetic properties of the particles were dominated by the shell. It is hypothesized, that this is because the shell was oxidized to a ferrimagnetic spinel phase, while the core remained an antiferromagnetic phase which did not contribute to the magnetization. CoFe + Mn has a manganese-rich shell, thus its magnetic properties were closer to manganese ferrite particles; however, MnFe + Co behaved more like cobalt ferrite since its cobalt-rich spinel shell governed its magnetic properties. To successfully make hard/soft, core/shell ferrite nanoparticles with this proposed seed-mediated drip method, an efficient oxidation strategy of the rock salt

Figure 8. ZFC/FC curves of CoFe + Mn and MnFe + Co samples. The blocking temperatures 184 ± 7 K (CoFe + Mn) and 251 ± 13 K (MnFe + Co), respectively. The insets showed the curves from 280 K to 330 K. Above 300 K, both samples showed higher ZFC magnetization than FC magnetization indicating a magnetostrictive property.

phase needs to be developed. There are a few candidate oxidation procedures developed previously [16, 46–48]. With an effective oxidation method, the particles can be transformed to a single spinel phase and the core/shell particles that exhibit exchange coupling effect can be synthesized.

4. Summary

In summary, we have successfully utilized a seed-mediated drip synthesis strategy to make manganese and cobalt substituted ferrite nanoparticles. The growth and elemental distribution were monitored during the synthesis and showed the potential using this technique to control the size and composition of ferrite nanoparticles. The size of the particles synthesized with this seed-mediated drip method was mostly determined by the seeding stage and the magnetic properties of the particles were determined by the dripping stage. Although a core/shell structure was not seen from the EDX mapping images, its existence was further inferred by other characterizations. The species of the precursors of the dripping stage determines whether the outer layer is rich in a specific metal element. The magnetic properties of the particles were more likely dominated by the more oxidized shell components, making the two samples with similar sizes have very different magnetic properties. The work to build more sophisticated structures and to achieve a deeper understanding of particle formation mechanisms during thermal decomposition is still in progress. With this work, further knowledge of the structure-property relationship of metal substituted ferrite nanoparticles will be obtained, which is important for the design of magnetic nanoparticles for various applications.

Data availability statement

All data that support the findings of this study are included within the article (and any supplementary files).

Acknowledgments

ORCID iDs

Zichun Yan ⬤ https://orcid.org/0000-0002-3755-8409
Sara FitzGerald ⬤ https://orcid.org/0000-0001-7907-2215
Thomas M Crawford ⬤ https://orcid.org/0000-0002-6986-7839
O Thompson Mefford ⬤ https://orcid.org/0000-0002-9164-2521

References

[1] Blanco-Andujar C, Walter A, Cotin G, Bordeianu C, Mertz D, Felder-Flesch D and Begin-Colin S 2016 Design of iron oxide-based nanoparticles for MRI and magnetic hyperthermia *Nanomedicine* **11** 1889–910

[2] Mohapatra J, Xing M and Liu J P 2019 Inductive thermal effect of ferrite magnetic nanoparticles *Materials* **12** 26–9

[3] Shin T H, Choi Y, Kim S and Cheon J 2015 Recent advances in magnetic nanoparticle-based multi-modal imaging *Chem. Soc. Rev.* **44** 4501–16

[4] Abenojar E C, Wickramasinghe S, Bas-Concepcion J and Samia A C S 2016 Structural effects on the magnetic hyperthermia properties of iron oxide nanoparticles *Prog. Nat. Sci. Mater. Int.* **26** 440–8

[5] Estelrich J, Escribano E, Queralt J and Busquets M A 2015 Iron oxide nanoparticles for magnetically-guided and magnetically-responsive drug delivery *Int. J. Mol. Sci.* **16** 8070–101

[6] Ling D and Hyeon T 2013 Chemical design of biocompatible iron oxide nanoparticles for medical applications *Small* **9** 9–10

[7] Nguyen D T and Kim K S 2016 Controlled magnetic properties of iron oxide-based nanoparticles for smart therapy *KONA Powder Part. J.* **2016** 33–47

[8] Lu A H, Salabas E L and Schüth F 2007 Magnetic nanoparticles: synthesis, protection, functionalization, and application *Angew. Chem., Int. Ed.* **46** 1222–44

[9] Kolhatkar A G, Jamison A C, Litvinov D, Willson R C and Lee R L 2013 Tuning the magnetic properties of nanoparticles *Int. J. Mol. Sci.* **14** 15977–6009

[10] Jana N R, Chen Y and Peng X 2004 Size- and shape-controlled magnetic (Cr, Mn, Fe, Co, Ni) oxide nanocrystals via a simple and general approach *Chem. Mater.* **16** 3931–5

[11] Xie W, Guo Z, Gao F, Gao Q, Wang D, Liaw B-S, Cai Q, Sun X, Wang X and Zhao L 2018 Shape-, size- and structure-controlled synthesis and biocompatibility of iron oxide nanoparticles for magnetic theranostics *Theranostics* **8** 3284–307

[12] Sun S, Zeng H, Robinson D B, Raoux S, Rice P M, Wang S X and Li G 2004 Monodisperse MFe_2O_4 (M = Fe, Co, Mn) Nanoparticles *J. Am. Chem. Soc.* **126** 273–9

[13] Park J, An K, Hwang Y, Park J-G, Noh H-J, Kim J-Y, Park J-H, Hwang N-M and Hyeon T 2004 Ultra-large-scale syntheses of monodisperse nanocrystals *Nat. Mater.* **3** 891–5

[14] Vreeland E C *et al* 2015 Enhanced nanoparticle size control by extending LaMer's mechanism *Chem. Mater.* **27** 6059–66

[15] Famiani S, Lagrow A P, Besenhard M O, Maenosono S and Thanh N T K 2018 Synthesis of fine-tuning highly magnetic $Fe@Fe_xO_y$ nanoparticles through continuous injection and a study of magnetic hyperthermia *Chem. Mater.* **30** 8897–904

[16] Unni M, Uhl A M, Savliwala S, Savitzky B H, Dhavalikar R, Garraud N, Arnold D P, Kourkoutis L F, Andrew J S and Rinaldi C 2017 Thermal decomposition synthesis of iron oxide nanoparticles with diminished magnetic dead layer by controlled addition of oxygen *ACS Nano* **11** 2284–303

[17] López-Ortega A, Estrader M, Salazar-Alvarez G, Roca A G and Nogués J 2015 Applications of exchange coupled bi-magnetic hard/soft and soft/hard magnetic core/shell nanoparticles *Phys. Rep.* **553** 1–32

[18] Liu F, Hou Y and Gao S 2014 Exchange-coupled nanocomposites: chemical synthesis, characterization and applications *Chem. Soc. Rev.* **43** 8098–113

[19] Moon S H, Noh S H, Lee J H, Shin T H, Lim Y and Cheon J 2017 Ultrathin interface regime of core–shell magnetic nanoparticles for effective magnetism tailoring *Nano Lett.* **17** 800–4

[20] Lee J H, Jang J-T, Choi J-S, Moon S H, Noh S-H, Kim J-W, Kim J-G, Kim I-S, Park K I and Cheon J 2011 Exchange-coupled magnetic nanoparticles for efficient heat induction *Nat. Nanotechnol.* **6** 418–22

[21] Robles J, Das R, Glassell M, Phan M H and Srikanth H 2018 Exchange-coupled $Fe_3O_4/CoFe_2O_4$ nanoparticles for advanced magnetic hyperthermia *AIP Adv.* **8** 2–8

[22] Gavrilov-Isaac V, Neveu S, Dupuis V, Taverna D, Gloter A and Cabuil V 2015 Synthesis of trimagnetic multishell $MnFe_2O_4@CoFe_2O_4@NiFe_2O_4$ nanoparticles *Small* **11** 2614–8

[23] Noh S H, Na W, Jang J-T, Lee J-H, Lee E J, Moon S H, Lim Y, Shin J-S and Cheon J 2012 Nanoscale magnetism control via surface and exchange anisotropy for optimized ferrimagnetic hysteresis *Nano Lett.* **12** 3716–21

[24] Fellows B D, Sandler S, Livingston J, Fuller K, Nwandu L, Timmins S, Lantz K A, Stefik M and Mefford O T 2018 Extended LaMer synthesis of cobalt-doped ferrite *IEEE Magn. Lett.* **9** 3–7

[25] Doebelin N and Kleeberg R 2015 Profex: a graphical user interface for the Rietveld refinement program BGMN *J. Appl. Crystallogr.* **48** 1573–80

[26] Bergmann J, Friedel P and Kleeberg R 1998 BGMN—a new fundamental parameters based Rietveld program for laboratory x-ray sources, its use in quantitative analysis and structure investigations *CPD Newslett. Commiss. Powder Diffract. Int Union Crystallogr.* **20** 5–8

[27] Zhang Q, Castellanos-Rubio I, Munshi R, Orue I, Pelaz B, Gries K I, Parak W J, del Pino P and Pralle A 2015 Model driven optimization of magnetic anisotropy of exchange-coupled core–shell ferrite nanoparticles for maximal hysteretic loss *Chem. Mater.* **27** 7380–7

[28] Song Q and Zhang Z J 2012 Controlled synthesis and magnetic properties of bimagnetic spinel ferrite $CoFe_2O_4$ and $MnFe_2O_4$ nanocrystals with core–shell architecture *J. Am. Chem. Soc.* **134** 10182–90

[29] Baaziz W *et al* 2014 Tuning of synthesis conditions by thermal decomposition toward core–shell $Co_xFe_{1-x}O@Co_yFe_{3-y}O_4$ and $CoFe_2O_4$ nanoparticles with spherical and cubic shapes *Chem. Mater.* **26** 5063–73

[30] Buck M R, Biacchi A J and Schaak R E 2014 Insights into the thermal decomposition of Co(II) oleate for the shape-controlled synthesis of wurtzite-type CoO nanocrystals *Chem. Mater.* **26** 1492–9

[31] Chen C J, Chiang R K, Lai H Y and Lin C R 2010 Characterization of monodisperse wüstite nanoparticles following partial oxidation *J. Phys. Chem. C* **114** 4258–63

[32] Lottini E, López-Ortega A, Bertoni G, Turner S, Meledina M, van Tendeloo G, de Julián Fernández C and Sangregorio C 2016 Strongly exchange coupled core|shell nanoparticles with high magnetic anisotropy: a strategy toward rare-earth-free permanent magnets *Chem. Mater.* **28** 4214–22

[33] Chen C J, Chiang R K, Kamali S and Wang S L 2015 Synthesis and controllable oxidation of monodisperse cobalt-doped wüstite nanoparticles and their core–shell stability and exchange-bias stabilization *Nanoscale* **7** 14332–43

[34] Bodnarchuk M I, Kovalenko M V, Groiss H, Resel R, Reissner M, Hesser G, Lechner R T, Steiner W, Schäffler F and Heiss W 2009 Exchange-coupled bimagnetic wüstite/metal ferrite core/shell nanocrystals: size, shape, and compositional control *Small* **5** 2247–52

[35] Baaziz W, Pichon B P, Fleutot S, Liu Y, Lefevre C, Greneche J-M, Toumi M, Mhiri T and Begin-Colin S 2014 Magnetic iron oxide nanoparticles: reproducible tuning of the size and nanosized-dependent composition, defects, and spin canting *J. Phys. Chem.* C **118** 3795–810

[36] Nedelkoski Z *et al* 2017 Origin of reduced magnetization and domain formation in small magnetite nanoparticles *Sci. Rep.* **7** 1–8

[37] Sharma S K, Vargas J M, Pirota K R, Kumar S, Lee C G and Knobel M 2011 Synthesis and ageing effect in FeO nanoparticles: transformation to core–shell FeO/Fe_3O_4 and their magnetic characterization *J. Alloys Compd.* **509** 6414–7

[38] Pichon B P *et al* 2011 Microstructural and magnetic investigations of wüstite-spinel core–shell cubic-shaped nanoparticles *Chem. Mater.* **23** 2886–900

[39] Bruvera I J, Zélis P M , Calatayud M P, Goya G F and Sánchez F H 2015 Determination of the blocking temperature of magnetic nanoparticles: the good, the bad, and the ugly *J. Appl. Phys.* **118** 184304

[40] Livesey K L, Ruta S, Anderson N R, Baldomir D, Chantrell R W and Serantes D 2018 Beyond the blocking model to fit nanoparticle ZFC/FC magnetisation curves *Sci. Rep.* **8** 1–9

[41] Liu C and Zhang Z J 2001 Size-dependent superparamagnetic properties of Mn spinel ferrite nanoparticles synthesized from reverse micelles *Chem. Mater.* **13** 2092–6

[42] Bibani M, Breitwieser R, Aubert A, Loyau V, Mercone S, Ammar S and Mammeri F 2019 Tailoring the magnetic properties of cobalt ferrite nanoparticles using the polyol process *Beilstein J. Nanotechnol.* **10** 1166–76

[43] Zhao B C, Ma Y Q, Song W H and Sun Y P 2006 Magnetization steps in the phase separated manganite $La_{0.275}Pr_{0.35}Ca_{0.375}MnO_3$ *Phys. Lett.* A **354** 472–6

[44] Salazar-Kuri U, Estevez J O, Silva-González N R and Pal U 2018 Large magnetostriction in chemically fabricated $CoFe_2O_4$ nanoparticles and its temperature dependence *J. Magn. Magn. Mater.* **460** 141–5

[45] Olabi A G and Grunwald A 2008 Design and application of magnetostrictive materials *Mater. Des.* **29** 469–83

[46] Hufschmid R, Arami H, Ferguson R M, Gonzales M, Teeman E, Brush L N, Browning N D and Krishnan K M 2015 Synthesis of phase-pure and monodisperse iron oxide nanoparticles by thermal decomposition *Nanoscale* **7** 11142–54

[47] Kemp S J, Ferguson R M, Khandhar A P and Krishnan K M 2016 Monodisperse magnetite nanoparticles with nearly ideal saturation magnetization *RSC Adv.* **6** 77452–64

[48] Lak A *et al* 2016 Facile transformation of FeO/Fe_3O_4 core–shell nanocubes to Fe_3O_4 via magnetic stimulation *Sci. Rep.* **6** 1–12